

1 Interferometric Meteor Head Echo Observations
2 using the Southern Argentina Agile Meteor Radar
3 (SAAMER)

D. Janches¹ and W. Hocking² and S. Pifko³ and J.L. Hormaechea⁴ and D.C.

Fritts⁵ and C. Brunini⁶ and R. Michell⁷ and M. Samara⁷

D. Janches, Space Weather Lab., Mail Code 674, GSFC/NASA, Greenbelt, MD 20771
(diego.janches@nasa.gov)

W. Hocking, Department of Physics and Astronomy, University of Western Ontario, Canada
(whocking@uwo.ca)

S. Pifko, Department of Aeronautics and Astronautics, Stanford University, CA, USA
(spifko@stanford.edu)

J. L. Hormaechea, Estacion Astronomica Rio Grande, Rio Grande, Tierra del Fuego, Argentina
(jlhor@earg.gov.ar)

D. C. Fritts, Gats Inc., Boulder CO, 8030 (dave@gats-inc.com)

C. Brunini, Departamento de Ciencias Astronomicas y Geofisicas, Universidad Nacional de La
Plata, La Plata, Argentina (claudiobrunini@yahoo.com)

R. Michell and M. Samara, SowthWest Research Institute, San Antonio, TX
(rmichell@swri.edu; msamara@swri.edu)

¹Space Weather Lab., Mail Code 674,

Abstract.

A radar meteor echo is the radar scattering signature from the free-electrons in a plasma trail generated by entry of extraterrestrial particles into the atmosphere. Three categories of scattering mechanisms exist: specular, non-specular trails, and head-echoes. Generally, there are two types of radars utilized to detect meteors. Traditional VHF meteor radars (often called all-sky radars) primarily detect the specular reflection of meteor trails traveling perpendicular to the line of sight of the scattering trail, while High Power and

GSFC/NASA, Greenbelt, MD 20771 USA

²Department of Physics and Astronomy,
University of Western Ontario, Canada

³Department of Aeronautics and
Astronautics, Stanford University, CA, USA

⁴Estacion Astronomica Rio Grande, Rio
Grande, Tierra del Fuego, Argentina

⁵Gats Inc., Boulder CO, 80301 USA

⁶Departamento de Ciencias Astronomicas
y Geofisicas, Universidad Nacional de La
Plata, La Plata, Argentina

⁷SowthWest Research Institute, San
Antonio, TX USA

12 Large Aperture (HPLA) radars efficiently detect meteor head-echoes and,
13 in some cases, non-specular trails. The fact that head-echo measurements
14 can be performed only with HPLA radars limits these studies in several ways.
15 HPLA radars are very sensitive instruments constraining the studies to the
16 lower masses, and these observations cannot be performed continuously be-
17 cause they take place at national observatories with limited allocated observ-
18 ing time. These drawbacks can be addressed by developing head echo observ-
19 ing techniques with modified all-sky meteor radars. In addition, the fact that
20 the simultaneous detection of all different scattering mechanisms can be made
21 with the same instrument, rather than requiring assorted different classes
22 of radars, can help clarify observed differences between the different method-
23 ologies. In this study, we demonstrate that such concurrent observations are
24 now possible, enabled by the enhanced design of the Southern Argentina Ag-
25 ile Meteor Radar (SAAMER) deployed at the Estacion Astronomica Rio Grande
26 (EARG) in Tierra del Fuego, Argentina. The results presented here are de-
27 rived from observations performed over a period of 12 days in August 2011,
28 and include meteoroid dynamical parameter distributions, radiants and es-
29 timated masses. Overall the SAAMER's head echo detections appear to be
30 produced by larger particles than those which have been studied thus far us-
31 ing this technique.

1. Introduction

32 The collision of asteroids and disintegration of comets are the main source of dust in the
33 Solar System. These processes give rise to a thick circumsolar disk of small debris known as
34 the Zodiacal Dust Cloud (ZDC). Several physical effects produced by larger Solar System
35 bodies result in the dust having relatively short lifetimes, maintaining a partial balance
36 in their distribution and preventing this cloud from becoming dustier. For example,
37 dust particles can be ejected from the Solar System by Jupiter, thermally obliterated by
38 the Sun, or physically fragmented by additional collisions amongst themselves. Also, a
39 portion of the cloud is swept up by the planets, and for the case of those with atmospheres
40 will produce the familiar phenomena of ionization and light production termed meteor.
41 We now know that similar processes occur in other systems as circumstellar disks of
42 dust have been observed, for example, around Beta Picoris [*Okamoto et al.*, 2004] and
43 Formalhaut [*Currie et al.*, 2012]. Thus, studying the ZDC enables the understanding of
44 its nature, shedding light into the history and development of the Solar System as well as
45 extra solar planetary environments [*Malhotra*, 1995; *Johansen et al.*, 2007; *Walsh et al.*,
46 2011; *Nesvorný et al.*, 2010; *Wiegert et al.*, 2009].

47 The ZDC is the source of meteoroids originating from the so-called Sporadic Meteor
48 Complex (SMC) formed by six apparent sources: Helion, Anti Helion, North and South
49 Apex and North and South Toroidal [*Jones and Brown*, 1993, and reference therein]. The
50 study of the ZDC, SMC and their relation is fundamental for a number of areas of re-
51 search within the Solar System and Planetary Sciences realms and many basic questions
52 regarding their nature still remain an unsolved puzzle [*Nesvorný et al.*, 2011b]. Issues

53 of importance include the relative contribution of comets and asteroids to the overall
54 dust budget, clarification of the dynamical processes that make particles of different sizes
55 produce the observed light scattering and thermal emissions, and the causes of the differ-
56 ences in relative strength of the sources [*Galligan and Baggaley, 2005; Campbell-Brown,*
57 *2008a, b; Brown and Jones, 1995; Galligan and Baggaley, 2005; Nesvorný et al., 2010;*
58 *Wiegert et al., 2009*]. In addition, the fact that knowledge of the ZDC can be utilized to es-
59 timate the amount of dust accreted by planets and satellites [*Nesvorný et al., 2010, 2011a*]
60 makes it a compelling tool for the additional study of the composition and chemistry of
61 planetary atmospheres. The daily ablation of billions of interplanetary dust particles
62 (IDPs) produces layers of neutral and ionized metal atoms in planetary atmospheres [e.g.
63 ~ 90 km of altitude on Earth and Mars, ~ 120 km on Venus; and ~ 550 km on Titan;
64 *Plane, 2003; Pätzold et al., 2005, 2009; Withers et al., 2008; Kliore et al., 2008*]. Once the
65 meteoric metals are injected into the atmosphere they are responsible for a diverse range
66 of phenomena, including: the formation of layers of metal atoms and ions, nucleation of
67 noctilucent clouds, impacts on stratospheric aerosols and O₃ chemistry, and fertilization
68 of the ocean with bio-available Fe, which has potential climate feedbacks [*Plane, 2003*].

69 Ground-based meteor observations with radars detect thousand of sporadic, as well as
70 shower, events every day, providing data sets with excellent statistics and a variety of
71 dynamical and physical information regarding the particles that produced the observed
72 meteors. This makes radar meteor science an optimal tool to study the ZDC. The radar
73 scattering signature produced by the interaction between the transmitted pulse and the
74 ionized region generated by entry of extraterrestrial particles into the atmosphere gives
75 rise to the radar meteor echo. Three categories of scattering mechanisms exist: specular

76 trails, non-specular trails, and head-echoes. Generally, there are two types of radars
77 utilized to detect meteors. Traditional VHF meteor radars (often called all-sky radars)
78 primarily detect the specular reflection of meteor trails traveling perpendicular to the
79 line of sight of the scattering trail while High Power and Large Aperture (HPLA) radars
80 efficiently detect meteor head-echoes and, in some cases, non-specular trails. Trails are
81 generally semi-stationary echoes that originate from the ionization left behind by the
82 meteoroid [Baggaley, 2002]. The specular or non-specular nature of the trails depends on
83 the viewing geometry and their position with respect to the magnetic field lines [Dyrud
84 *et al.*, 2002]. While specular trails produce echoes that are confined to one altitude,
85 non-specular reflections occur from Field Align Instabilities (FAIs) that are spread in
86 many range gates. Head-echoes, on the other hand, are reflections from the plasma
87 immediately surrounding the meteoroid itself traveling at, or near, its speed [Janches
88 *et al.*, 2000a, 2003].

89 The first head echo detection was reported by *Hey et al.* [1947] who made observa-
90 tions with a 150 kW VHF radar system during the Giacobinid meteor storm of 1946,
91 while *Evans* [1965] used the Millstone Hill incoherent scatter radar system to conduct the
92 first head echo measurements using HPLA radars. However, routine operational world-
93 wide head echo observations utilizing HPLA radar only began in earnest almost 3 decades
94 later [Pellinen-Wannberg and Wannberg, 1994; Mathews *et al.*, 1997; Close *et al.*, 2000;
95 *Sato et al.*, 2000; Chau and Woodman, 2004; Janches *et al.*, 2006; Sparks *et al.*, 2009].
96 Because head echoes allow direct detection of the meteoroid flight in the atmosphere, they
97 provide information about meteoroid changes during the actual entry process, and so pro-
98 vide key information for understanding mass loss mechanisms [Kero *et al.*, 2008; Janches

99 *et al.*, 2009], electromagnetic plasma processes [*Dyrud et al.*, 2002], as well as enabling
100 the quantification of the mass range of detected particles [*Close et al.*, 2012] and their
101 effect in the upper atmosphere [*Fentzke and Janches*, 2008; *Gardner et al.*, 2011]. HPLA
102 radars are characterized by their high peak transmitter power (≥ 1 MW) at VHF and UHF
103 frequencies that range between 50 and 1200 MHz, and antenna apertures, in the form of
104 arrays or dishes, that have areas ranging between $\sim 800-9 \times 10^4$ m² [*Janches et al.*, 2008,
105 see also Section 5 and Table 2]. This focuses most of the radiation into narrow beams
106 with patterns characterized by Full Width Half Maximum (FWHM) between 0.16 and
107 3 degrees. In comparison, meteor radars generally transmit with a single Yagi or dipole
108 antennas at VHF frequencies ranging from 17 to 50 MHz and peak power of the order of
109 6–20kW [*Galligan and Baggaley*, 2004; *Brown et al.*, 2008; *Younger et al.*, 2009]. Thus,
110 over the past decade, two distinct areas of research have developed separately in radar me-
111 teor science. The first one is based on the more classical detection of specular reflections
112 of meteor trails using meteor radars and the second is based on detection of head echoes
113 and non specular trails utilizing HPLA radars. Results from both areas have shown sig-
114 nificantly different observed meteoroid dynamical property distributions [*Janches et al.*,
115 2008] and trying to elucidate the origins of these differences has been a major undertake.

116 The fact that head-echo measurements can be performed only with HPLA radars limits
117 these studies in several ways. HPLA radars are very sensitive instruments constraining
118 the studies to the lower masses within the spectrum of terrestrial atmospheric aeronom-
119 ical interest [*Mathews et al.*, 2001]. In addition, meteor observations with HPLA radars
120 are scarce because they are radars at national observatories, and as such the allocated
121 observing time in these instruments is limited. To date, only the Arecibo and MU radars

has been used extensively to study seasonal effects in the observed meteor flux properties [Janches *et al.*, 2006; Kero *et al.*, 2011]. If head echo detections can successfully be made with meteor radars, such observations can potentially address these limitations. In addition, the fact that the detection of all different scattering mechanisms, only possible now using an assorted class of radars, can be made with the same instrument can contribute to the explanation of the observed differences. Thus in this manuscript we demonstrate that such observations are now possible with the Southern Argentina Agile Meteor Radar (SAAMER) enabled by its enhanced design. Section 2 discusses in detail the system characteristics while Section 3 describes our data analysis methodology. In Section 4 we present a summary of the most representative results and distributions from the head echo observations utilizing SAAMER, and compare them with past HPLA radar observations in Section 5. In particular we will compare our results with the Arecibo 430 MHz radar in Puerto Rico, The 440 MHz Poker Flat Incoherent Scatter Radar (PFISR) in Alaska, the 46 MHz Middle and Upper (MU) radar in Japan, the 160 MHz ARPA Long-Range Tracking and Instrumentation Radar (ALTAIR) in the Marshall Islands, and the 50 MHz Jicamarca radar in Peru.

2. SAAMER: System description

SAAMER is a SKiYMET system [Hocking *et al.*, 1997] deployed at the Estacion Astronomica Rio Grande (EARG) in the city of Rio Grande ($53.8^{\circ} 45' 8''$ S; $67^{\circ} 45' 5''$ W), province of Tierra del Fuego, Argentina. SAAMER has been operational continuously since May, 2008 at a frequency of 32.55 MHz. It is enhanced relative to standard meteor radars, in order to enable Gravity Wave (GW) momentum flux measurements in the Mesosphere and Lower Thermosphere (MLT) atmospheric region [Fritts *et al.*, 2010a, b]. These

144 enhancements over the more traditional systems were driven by two important new re-
145 quirements: 1) the need for significantly higher count rates and 2) a need for the majority
146 of meteor detections to be at small zenith (high elevation) angles. Both needs were ad-
147 dressed with SAAMER, which additionally was designed for greatly enhanced transmitter
148 peak power (60 kW, rather than 6-20 kW used by most meteor radar systems).

149 Of particular interest for this work, is that SAAMER uses a transmitter phase an-
150 tenna array configuration, specially designed by Mardoc Inc., composed of eight 3-element
151 crossed yagis arranged in an octagon of 27.6 m (3 wavelengths) in diameter (Figure 1).
152 This is significantly different from typical systems, which use a single antenna. In addi-
153 tion, the ability to change electronically (e.g. pulse to pulse) the phases between antennas
154 provides great flexibility to the system, since it allows transmission with different radiation
155 patterns and hence permits performance of a number of different experiments. This makes
156 SAAMER not only an operational instrument but also a system with which additional
157 radar experiments can be implemented.

158 In the normal mode of operation (hereafter referred as Mode 1), designed to measure
159 mesospheric winds, SAAMER transmits with opposite phasing of every other yagi, di-
160 recting the majority of radar power into eight beams at 45° azimuth increments with
161 peak power at $\sim 35^\circ$ off zenith (Figure 2a). This results in a majority of meteor specular
162 trail detections at off-zenith angles between 15° and 50° [Fritts *et al.*, 2012a]. During the
163 first 16 months of operation, SAAMER transmitted a 2-km ($13.4 \mu\text{s}$) long monopulse at
164 2140 Hz pulse repetition frequency (PRF) and a bandwidth of 0.3 MHz resulting in an
165 excess of 10,000 meteor trail specular reflections detected daily. In September of 2009,
166 however, the transmitting scheme was changed to a 2-bit Barker code pulse of total length

167 of 26.8 microsec at a PRF of 1765 Hz. This change resulted in a $\sim 40\%$ increase in the
168 daily counts, that is in 15,000 to 25,000 daily detected underdense specular meteor trail
169 events [*Janches et al.*, 2012].

170 For the purpose of the work described herein, enabled by the agility of SAAMER’s new
171 transmitter design, we utilized a transmitting mode that somewhat follows the methodol-
172 ogy applied in the past for meteor head echo observations utilizing HPLA radars (hereafter
173 called Mode 2). As opposed to the semi-stationary nature of specular reflections from me-
174 teor trails, the head echo originates from the plasma surrounding the meteoroid, moving
175 at or near its speed [*Janches et al.*, 2000a]. Its radar cross section is much smaller than the
176 trail [*Close et al.*, 2004], requiring far better detection sensitivity as well as improved tem-
177 poral resolution. For these reasons, Mode 2 transmits with all the TX antennas in Phase
178 resulting in most of the radiated power upwards in a relatively, narrow beam [*Janches*
179 *et al.*, 2000b, 2002, 2003; *Sparks et al.*, 2009; *Pifko et al.*, 2012]. As displayed in Figure 2b,
180 Mode 2 results in a near Gaussian central transmitted beam pattern with a 3 dB decrease
181 in gain at $\sim 8^\circ$. We refer to this mode as a “relatively” narrow beam because when com-
182 pared with HPLA systems, SAAMER’s main beam width is approximately 3 times wider
183 than the MU and ALTAIR radars [*Close et al.*, 2000; *Kero et al.*, 2011], 8 times wider
184 than PFISR and Jicamarca [*Chau and Woodman*, 2004; *Sparks et al.*, 2010] and 50 times
185 wider than the Arecibo radar [*Janches et al.*, 2004], yet is much narrower than the typical
186 all-sky pattern resulting from a single yagi antenna utilized in most of the meteor radar
187 systems [*Fritts et al.*, 2012a]. Specifically, we transmitted a $13.5 \mu\text{s}$ monopulse at a PRF
188 of 500 Hz and performed a 2 point pulse coherent integration, thus resulting in an effective
189 Interpulse period (IPP) of 4 msec. The sampling resolution of the return signal was 250 m

190 and the bandwidth was 0.05 MHz. The vertical altitude range covered was between ~ 75
191 km and 130 km. Table 1 presents a summary of SAAMER’s operation characteristics in
192 Mode 2. As it will be discussed in more detail in the following sections, the larger area
193 and lower transmitted power, as compared to HPLA systems, will result in lower power
194 density which will result in sensitivity to larger particles than those detected by HPLA
195 radars. Hence the ability to utilize SAAMER in head-echo observing mode extends the
196 size range of meteoroids for which this technique can be applied.

197 The data presented in this paper were obtained during an observing campaign performed
198 between August 2 and 14, 2011. During that time we also performed simultaneous optical
199 observations that will be presented in a future paper. We transmitted in Mode 2 generally
200 from evening hours until noon so as to cover the early morning meteor rate rise and
201 peak [*Janches et al.*, 2006]. The return echoes are received by both the TX array and the
202 receiving (RX) array, where the latter is formed by a modified version of the typical five
203 antennas interferometer arrangement [Figure 1, *Hocking et al.*, 1997], all of which are also
204 3 – element crossed yagis. Due to physical constrains at the location where SAAMER
205 operates, the southernmost RX antenna was shifted off the cross axis toward the east by a
206 distance equal to a wavelength. Such modification preserves all the characteristics of the
207 interferometric antenna arrangement developed by *Hocking et al.* [1997] and demonstrates
208 that the “cross” arrangement is just one of many antenna positioning options available
209 to form a RX interferometer that enables redundant position definition of the detected
210 echoes. For example, a clone system to SAAMER operating in the Brazilian Antarctic
211 Base Comandate Ferraz in King George Island uses a “T” antenna arrangement [*Fritts*
212 *et al.*, 2012b]. Using the interferometer, the position for each detected range gate at every

213 IPP is determined with errors less than 0.5° , ultimately enabling the determination of
214 absolute meteoroid velocities as discussed in the next section.

3. Data Analysis

215 SAAMER uses the basic real-time echo detection and analysis algorithms for the
216 SKiYMET systems developed by *Hocking et al.* [2001], independently of what transmitting
217 mode is been utilized. These algorithms simultaneously stream raw data into memory,
218 detect occurrences of meteors and identify and store those produced by underdense spec-
219 ular reflections [*McKinley*, 1961; *Ceplecha et al.*, 1998]. From these selected events, the
220 location of meteor trails (range and angle) are determined, as well as their radial drift
221 speeds and decay times. Underdense specular meteor trail events are semi-stationary tar-
222 gets drifting with the background wind at speeds that range typically from a few to ~ 100
223 m/s. Thus, when analyzing raw data, these events are detected in the same range gate
224 during many IPPs until the returned signal strengths falls below the noise floor due to
225 their diffusion in the background atmosphere [*Lau et al.*, 2006]. Head echoes, on the other
226 hand, move at hypersonic speeds (\sim km/sec) and therefore they will be detected over
227 several range gates with increasing time (i.e. IPP) [*Janches et al.*, 2000a]. Thus, for the
228 case of this work, additional data analysis and processing were required to be performed
229 off line. For this, we recorded the in-phase and quadrature components of the voltage of
230 the returned signal for each range gate, coherently integrated over 2 IPPs for each of the
231 6 receiving channels, five from each of the antennas that form the RX array and one from
232 the TX array used as a receiver. Initially, we performed a running average of the noise
233 floor and searched through the raw data for enhancements greater than 3 sigmas above
234 the noise. Due to the presence of thousands of trail events which are detected hourly by

235 SAAMER, this simple approach is not efficient for identification of single head echoes,
236 requiring that we perform a visual inspection among the detected candidates. Figures 3
237 and 4 show the Range-Time-Intensity (RTI) images for two examples of such events. The
238 first five panels from each figure correspond to the data recorded on each of the RX array
239 antenna. The sixth panel corresponds to data recorded with the 8-Yagi TX array utilized
240 as a receiver. A common feature of the radars is that the echo return is range aliased
241 and, for the case of meteor radars, the interferometric results as well as the assumption
242 that meteors occur between 70 and 140 km of altitudes are needed to obtain the corrected
243 altitudes. This step is not yet applied for the data presented in Figures 3 and 4 and that
244 is why the vertical axis show uncorrected ranges.

245 Once the head echo events had been identified we proceeded to determine the mete-
246 roid motion vector. For this, we performed interferometric calculations for every IPP by
247 determining the phase differences between receiving channels for a selected range gate.
248 As can be seen from the detailed RTI images displayed in Figures 5 of the two examples
249 shown in Figures 3 and 4, for a given IPP, the events show a vertical spread of range gates
250 which in many cases is longer than the pulse length. We then determine, for each IPP in
251 which the meteor is present, the lowest range gate of the vertical signal range spread (i.e.
252 leading edge) and select among ten range gates (about the length of the pulse in ranges)
253 from the lowest one, the gate with maximum signal strength. This is represented by the
254 black dots in this figure. The use of the 5 antenna interferometer arrangement allows for
255 the unambiguous determination of the spatial location for each IPP. This methodology is
256 widely utilized and will not be described in this work. *Hocking et al.* [1997] and *Hocking*
257 *et al.* [2001] described in detail the operation of the 5 antenna meteor radar interferome-

258 ter. The application of interferometry for head echo purposes has been reported by *Sato*
259 *et al.* [2000]; *Chau and Woodman* [2004]; *Hunt et al.* [2004] and *Sparks et al.* [2010]. The
260 results of the inteferometry calculation for both examples are displayed in Figure 6 where
261 the vertical, eastward and northward positions for each IPP are shown as black dots. It is
262 evident from these panels that the interferometric results are noisier than those reported
263 in the past by HPLA radars [*Sparks et al.*, 2010, and reference therein]. However, a clear
264 trend is present in the data and a linear fits can be applied in order to obtain an estimate
265 of each component of the vector velocity. An interesting point to note from these pan-
266 els is that both events were detected at heights greater than 110 km, somewhat greater
267 than average altitudes reported in previous HPLA observations [~ 105 km *Janches et al.*,
268 2002, 2003; *Sparks et al.*, 2009; *Pifko et al.*, 2012]. In addition, the distance traveled in
269 some of the planes, in some cases greater than 10 km, are relatively larger than previous
270 HPLA observations. Although some dependency on the lower transmitted frequency and
271 radar beam size exists, both factors also suggest that these head echoes are produced by
272 relatively larger particles than those detected by HPLA systems [*Janches et al.*, 2008;
273 *Pifko et al.*, 2012]. In the next section we present a summary of the results obtained
274 throughout the observing campaign.

4. Results

275 As described in Section 2, the data presented in this work were obtained over a period
276 of 12 days covering August 2 to 14, 2011. Due to the low sensitivity of SAAMER,
277 we did not expect meteor head-echo detection rates to be as large as is the case for
278 HPLA radars. In addition, because these observations were performed simultaneously
279 with an optical campaign aimed at observing the same events with radar and optical

280 techniques, we concentrated mostly on night hours, with the inclusion of mornings to
281 cover the flux rate increase and peaks [*Janches et al.*, 2006], thus increasing the likelihood
282 of successful observations. Figure 7 displays the observing interval times for each day of
283 observations. Figure 8 provides information on the head echo detection rate observed by
284 SAAMER. Over the 12 days of observations, an average of ~ 15 head echoes were observed
285 (Figure 8a) during each observing period that lasted on average ~ 14 hrs (Figure 8b),
286 resulting in, approximately, one detection every hour (Figure 8c). Figure 8d displays the
287 number of head echoes detected through out the day for all the days combined. Although
288 observations were stopped after local noon (Figure 7), Figure 8d indicates that most of the
289 detections occur between 5 am and noon, consistent with the diurnal behavior of meteor
290 head echoes observed by radars [*Janches et al.*, 2006; *Fentzke et al.*, 2009; *Sparks et al.*,
291 2009]. As can be derived from Figure 8, the SAAMER head echo detection rate is up to
292 2 order of magnitude lower than those resulting from HPLA radar observations [*Janches*
293 *et al.*, 2006; *Sparks et al.*, 2009; *Pifko et al.*, 2012]. Although the much reduced detection
294 rate is in part due to the significantly lower sensitivity of SAAMER compared to that of
295 HPLA systems, this is also indicative that the particles producing SAAMER's detected
296 head echoes may be significantly larger than those detected by HPLA radars [*Janches*
297 *et al.*, 2008; *Fentzke et al.*, 2009; *Pifko et al.*, 2012]. First, larger particles will produce
298 larger electron concentrations, so that they may be detected by the lower sensitivity
299 SAAMER system [*Fentzke and Janches*, 2008], and second, the influx rate of meteoroids
300 decreases with increasing size resulting in the lower detected rate [*Ceplecha et al.*, 1998].
301 In addition, it is worth noting that these observations were performed near the southern
302 hemisphere spring equinox, which according to models and observations is the period

303 during which the meteor count-rates reach a minimum at a given location [*Janches et al.*,
304 2006]. This seasonal variability is enhanced, in particular, at higher latitudes [*Sparks*
305 *et al.*, 2009]. Thus it is likely the observed rate may increase significantly during the fall
306 equinox period.

307 Figure 9a presents the initial meteor head echo altitude distribution, that is the altitude
308 at which the first meteor IPP is recorded [*Janches and ReVelle*, 2005]. Although the
309 counts are low, limiting statistical reliability, (in particular when compared with HPLA
310 observations), a peak at about ~ 110 km of altitude is evident from this figure. In addition,
311 more than 45% of SAAMER's detections are between 110 and 120 km. Both the peak as
312 well as the large percentage of high altitude events are significantly higher than similar
313 studies utilizing HPLA observations [*Chau and Woodman*, 2004; *Janches et al.*, 2003;
314 *Chau et al.*, 2007; *Sparks et al.*, 2009; *Pifko et al.*, 2012; *Close et al.*, 2012]. One must be
315 cautious when doing these comparisons, however, due to the large differences in system
316 sensitivity, transmitted frequency and even detected particle size range. We will discuss
317 this in more detail in the next section.

318 The geocentric velocity distribution resulting from SAAMER's head echo observations
319 is presented in Figure 9b. Due to the low statistical sample a clear distribution shape is
320 not evident from this panel. However a slight dominance of higher velocities (≥ 30 km/sec)
321 meteors can be observed that is generally typical of head-echo observations [*Janches et al.*,
322 2003; *Janches et al.*, 2008; *Sparks et al.*, 2010; *Pifko et al.*, 2012]. Uncertainties of these
323 estimates are obtained by propagating the errors of the individual linear fits (Figure 6).
324 Overall, the methodology presented here provides the absolute velocity estimates with
325 errors of the order of a few to 20 %, with a few cases with higher errors. This is observed

326 in Figure 10 where the distribution of the absolute velocity uncertainty is displayed. The
327 median in this distribution results in 14.6 %. Also, Figure 9b, shows the presence of
328 a few meteor samples with velocities greater than the Solar System escape velocity (i.e.
329 72 km/sec). These particles are also seen in HPLA observations, specially those with
330 interferometric capabilities [*Sato et al.*, 2000; *Chau and Woodman*, 2004; *Chau et al.*,
331 2007; *Pifko et al.*, 2012]. There are many factors that can produce such detections, such
332 as inaccuracies in the observing methods, acceleration processes due to the giant planets,
333 and indeed true interstellar origin. This issue however, is currently beyond the scope of
334 this investigation.

335 The horizontal projections of the vector velocities are displayed in Figure 11. The circles
336 in these figure represent 5, 10 and 20 degrees off zenith at ~ 110 km of altitude. As can be
337 observed from this figure, most of the detection occurred overhead within 10 degrees off
338 zenith which is the region of higher transmitted power density, with no detections beyond
339 20 degree of zenith, from any of the side lobes (Figure 2b). It is important to note that the
340 horizontal projections displayed in Figure 11 are unambiguous meteor positions. This is
341 possible due the use of the five antenna interferometer [*Jones et al.*, 1998]. Furthermore,
342 it can be derived from Figure 11, that most of these observations are relatively long lived,
343 compared to other HPLA observations, with some events producing significant amount
344 of electrons along distances greater than 20 km. This can also be seen in more detail in
345 Figure 12, where distributions of the horizontal, vertical and absolute distances through
346 which the meteor is observed are displayed. In particular, it can be seen in the third
347 panel of Figure 12 that the majority of observed meteors have typical vertical extents of
348 between half to one atmospheric scale height at those altitudes ($\sim 7 - 10$ km). This once

349 again suggests the these meteors are produce by large meteoroids, as will be discussed in
350 the next section.

351 As a final measured result reported in this section, we present the distribution of the
352 meteor entry angles (i.e. the zenith angle of the meteoroid trajectory) derived from
353 the velocity components, This distribution is displayed in Figure 13. In the figure, an
354 entry angle of 0° corresponds to a trajectory that was aligned with the local vertical (i.e.
355 the meteoroid was travelling straight downward), while 90° corresponds to a horizontal
356 velocity vector. The results in this figure indicate that most of the observations are
357 produced by particles entering at angle smaller or equal to 45° with respect to the local
358 zenith. A sharp decrease of meteoroids entering the atmosphere at higher angle values then
359 occurs, and almost no particles with angles higher than ~ 75 degrees. This observation
360 agrees with past modeling results reported by *Janches et al.* [2006]; *Fentzke and Janches*
361 [2008] and *Fentzke et al.* [2009]. In order to obtain agreements between modeled and
362 observed head echo rates by different radars and locations, those authors argued for the
363 need to reject most of the meteoroids entering at these large zenith angles. Recently, *Pifko*
364 *et al.* [2012] reported interferometric measurements of head echoes using the MU radar
365 in Japan and showed similar results, where the number of meteors decrease rapidly for
366 entry angles greater than $\sim 60^\circ$, and incoming meteors at angles of $\geq 75^\circ$ are, in practical
367 terms, negligible.

5. Discussion

368 In Section 4 we presented a summary of the most representative results and distributions
369 from the head echo observations utilizing SAAMER. In this section we discuss these results
370 in the context of previous head-echo observations utilizing HPLA radars and determine

371 how SAAMER's observations compare to and/or complement those obtained with the
 372 more powerful and sensitive systems. In Section 2 we discussed the difference in beam
 373 width between SAAMER's transmitting in Mode 2 and HPLA radars and argued that
 374 SAAMER's wider beam will result in sensitivity to larger particles than those generally
 375 detected by HPLA radars. We will now attempt to quantify this hypothesis. Table 2
 376 presents a comparison of several figures of merit between SAAMER and a selected group
 377 of HPLA systems for which meteor head echo observations have been performed and
 378 reported repeatedly (column 1). Columns 2 and 3 list the radar operating wavelength
 379 and frequency while the fourth column provides the peak transmitted power. Note that
 380 even though SAAMER is a high power system when compared to other all-sky meteor
 381 radars, it is still 2 orders of magnitude lower than any of the more powerful HPLA radars.
 382 The fifth column provides the aperture of each radar. For the case of SAAMER we
 383 calculate its aperture as the area in a circle of diameter equal to 3λ . MU, ALTAIR and
 384 Arecibo are also circular areas with diameters equal to 103, 46 and 300 m respectively.
 385 PFISR and Jicamarca are rectangular areas with dimensions equal to 27.5×31.5 m and
 386 300×300 m respectively. If we assume that this aperture is the effective aperture, A_{eff} ,
 387 we can then calculate the Gain (G) as

$$G = 4\pi \frac{A_{eff}}{\lambda} \quad (1)$$

388 This quantity is listed in the sixth column. The last column of Table 2 provides the power
 389 density (P_d) calculated from

$$P_d = \frac{P_t \times G}{4\pi \times R^2} \quad (2)$$

390 where R is range chosen to be 110 km for this comparison. We note that, for the case of
 391 SAAMER, this may result in an overestimation of its aperture because the array is only
 392 sparsely filled, but even if its A_{eff} is reduced to half, it will result in only a 3 dB decrease
 393 in G (~ 7.3 dB), which is comparable to the gain of a single 3-element Yagi antenna, and
 394 a one order of magnitude decrease in P_d . Thus, for the purpose of this discussion, we
 395 believe that the results presented in Table 2 are reasonable representations of SAAMER’s
 396 “best case scenario” performance.

397 If we utilize P_d as a proxy for the radar sensitivity for the case of head echo observations,
 398 the results in Table 2 show that while there is a variability of 3 orders of magnitude of
 399 this value among the HPLA systems, SAAMER differs by 4 to 7 orders of magnitude with
 400 respect to these sensitive instruments. Thus while there may be an overlap between the
 401 meteoroid mass range detected by each of the HPLA radars, the much smaller sensitivity
 402 of SAAMER suggests that the particles producing the head echoes reported here must be a
 403 different class (i.e. larger). Recently, *Pifko et al.* [2012] reported a comparison of detected
 404 sensitivity as a function of meteoroid mass between the Arecibo, PFISR, MU and ALTAIR
 405 radars. Utilizing the head echo Radar Cross Section (RCS) model developed by *Close et al.*
 406 [2005] combined with the same radar sensitivity approach introduced by *Janches et al.*
 407 [2008], the authors estimated the minimum velocity that a meteoroid with a given mass
 408 must have to be detected by any of these radars, and the results are reproduced in Table 3.
 409 As described by *Close et al.* [2005], the model and, therefore, determined sensitivity is
 410 strongly dependent on radar frequency. Taking this into account, we first concentrate on

411 the UHF frequencies by comparing Arecibo and PFISR. Both radars transmit essentially
412 the same frequency (430 and 440 MHz respectively), have a 2 order of magnitude difference
413 in P_d (Table 2) and 1 order of magnitude difference in meteoroid mass sensitivity (Table 3).
414 That is, PFISR can detect meteoroids traveling at 15 km/sec with masses equal to 10 μg ,
415 unlike Arecibo, which can detect meteoroids at the same velocity but smaller in mass by
416 an order of magnitude. A similar trend can be observed for VHF frequencies when we
417 compare MU and ALTAIR, although caution must be taken in this case because their
418 frequencies are significantly different. This indicates that, given a meteoroid velocity, a
419 difference of two orders of magnitude in radar P_d translates to one order of magnitude in
420 mass range detected sensitivity. Applying this conjecture to SAAMER and utilizing MU
421 as a reference, since their frequencies are comparable, we can estimate that SAAMER
422 will be able to detect particles with minimum masses of the order of $10^2 \mu\text{g}$ if the particle
423 travels at very high speeds (~ 60 km/sec) and $10^4 \mu\text{g}$ if they travel at 15 km/sec.

424 On the other hand, because the number of meteors per unit area per unit time decreases
425 as the particle mass increases [Cepilecha et al., 1998], the maximum mass that each of these
426 radars can detect will be limited by their beam size. For example, Fentzke and Janches
427 [2008] and Fentzke et al. [2009] determined, using modeling and observed results, that
428 Arecibo's detected mass range, considering all velocities, is 10^{-4} to 10 μg while PFISR's
429 will be 1 to 250 μg . Similarly, Pifko et al. [2012] determined a detected mass range by
430 the MU radar of also 1 to 250 μg . This agrees with recent results reported by Kero et al.
431 [2011] who, utilizing RCS calculations, determined a MU detected mass range of 1 to
432 1000 μg . For the case of ALTAR, Close et al. [2012] estimated a detected mass range
433 between 1 to $10^4 \mu\text{g}$ utilizing an improved technique for calculating bulk densities of low-

434 mass meteoroids using a plasma scattering model. Given the very small collecting area
435 of ALTAIR's VHF system (beam width $\sim 2.8^\circ$), it is somewhat surprising to see detection
436 of particles greater than $1000 \mu\text{g}$ if we assume the mass flux reported by *Ceplecha et al.*
437 [1998] to be correct. However, when looking at the mass distribution in detail, the number
438 of particles decreases abruptly for masses greater than $10^2 \mu\text{g}$ and values larger than those
439 are simply part of the distribution tail ($\leq 15\%$, S. Close, Personal Communication, 2012),
440 which suggests they can be outliers of the model. In any case, it is evident that the
441 minimum masses determined to be detected by SAAMER are equal or greater than the
442 maximum masses detected by HPLA radars as reported by these various authors, and
443 that overall the SAAMER's head echo detections are produced by larger particles than
444 those which are commonly studied using this technique.

445 As a final result, we present meteoroid radiant information enabled by the interferomet-
446 ric determination of the vector velocity. Until now, this has only been possible utilizing
447 the ALTAIR, Jicamarca, MU and PFISR radars [*Sato et al.*, 2000; *Hunt et al.*, 2004; *Chau*
448 *and Woodman*, 2004; *Chau et al.*, 2007; *Sparks et al.*, 2010; *Kero et al.*, 2011; *Pifko et al.*,
449 2012]. Figure 14 displays the calculated meteoroid radiant color coded to their velocity
450 plotted in terms of Sun-centered ecliptic longitude ($\lambda - \lambda_0$) and latitude (β). These data
451 represent the point in the sky that the meteoroids entered into a hyperbolic geocentric
452 orbit [*Jones and Brown*, 1993]. The radiant angles are defined such that the ecliptic lon-
453 gitude is the angle of rotation about the ecliptic normal measured from the Earth-Sun
454 direction, and the ecliptic latitude is the angle of rotation out of the ecliptic plane (i.e.,
455 the Sun is located at $\lambda - \lambda_0 = 0^\circ$, $\beta = 0^\circ$). The plots in Figure 14 are oriented such that
456 the center point corresponds to the Apex direction (i.e., the direction of Earth's velocity

relative to the Sun). The locations of the six sporadic meteoroid sources are also displayed
in the figure as ellipses, with the coordinates as specified in *Pifko et al.* [2012]. The North
and South Apex (NA and SA) sources lie just above and below the figure center point,
respectively. Likewise, the North and South Toroidal (NT and ST) sources are above and
below the respective Apex sources. To the left of the Apex is the Helion (H) direction,
and the Anti-Helion (AH) is symmetrically opposite to the Helion source about the Apex.
As expected given SAAMER's location and the time period during which these observa-
tions were performed, the majority of the detections appear to come from the SA and ST
source region and a minority originating from the NA and AH regions. Note that most of
the radiants lie below 30° in ecliptic latitude, which is expected due to SAAMER's high
southern geographical latitude.

6. Conclusions

We have presented meteor head echo observations using SAAMER and demonstrated
that, enabled by the enhanced design of this system compared to typical meteor radars,
studies that are not based on the commonly detected specular trails are possible. There
are many reasons why these results are compelling. Over the past decade, stud-
ies of the microgram-size meteoroid mass input in the upper atmosphere have bene-
fited tremendously with the introduction of meteor head echo observations using HPLA
radars [*Janches et al.*, 2008]. These observations have enabled us to develop and validate
modeling essential for our understanding of the temporal and spatial variability of the
meteoric flux, physical characteristics of the meteors and meteoroids, and how they relate
to layered phenomena in the Earth's mesopause region [*Janches et al.*, 2006; *Fentzke and*
Janches, 2008; *Fentzke et al.*, 2009; *Plane et al.*, 2010; *Gardner et al.*, 2011]. Further-

479 more, these highly resolved measurements have contributed to identifying the mass loss
480 mechanisms that these particles undergo upon atmospheric entry, allowing us to relate
481 small scale features of the detected radar light curves with the precise moment that a
482 particular chemical constituent is released from the meteoroid body [*Dyrud and Janches,*
483 2008; *Janches et al., 2009; Close et al., 2012*]. The fact that these measurements can be
484 performed only with HPLA radars limits these studies in several ways. First, since HPLA
485 radars are very sensitive instruments, the studies are generally constrained to the lower
486 masses within the spectrum of Terrestrial atmospheric aeronomical interest. Secondly,
487 meteor observations with HPLA radars are scarce because they are made at national ob-
488 servatories and as such the allocated observing time on these instruments is shared among
489 many other type of experiments. In fact, only the Arecibo and MU radars have been used
490 extensively to study seasonal effects in the observed meteor diurnal properties [*Kero et al.,*
491 2011; *Pifko et al., 2012; Janches et al., 2006*]. The routine utilization of enhanced me-
492 teor radars, such as SAAMER, to observe and detect head echoes addresses both issues.
493 First we have shown that the observational technique can be extended to larger masses,
494 expanding the mass range of particles that can be studied using the same methodology.
495 Second, these systems, even with SAAMER's enhancements, are two to three orders of
496 magnitude less expensive than HPLA radars, in addition to being easily deployable and
497 almost 100% autonomous. That implies that these observations can be performed contin-
498 uously and the potential for more deployments at different locations is attainable. This
499 also addresses the low detection rate drawback, since 24 hr long observation periods may
500 not provide a statistical significant sample, a problem at this mass range, but because
501 these instruments are operated continuously the collection of large data sets over long

502 periods of time is now possible. A methodology to achieve this objective is under current
503 development.

504 In addition to measurements of the head-echo, HPLA radars have been instrumental in
505 the detection and understanding of the plasma phenomena surrounding the non-specular
506 (i.e. field aligned) meteor trails [*Dyrud et al.*, 2002, 2007a, b]. Although most of the
507 HPLA radars can be used to detect head-echoes, only three [out of 11; *Janches et al.*,
508 2008] can successfully detect non-specular trail echoes, all of which are at low to mid
509 latitudes (ALTAIR in the Marshall Islands, the MU radar in Japan and the Jicamarca
510 radar in Peru). The characteristics of these echoes (i.e. duration, spatial extend, etc),
511 which provide key information on meteoroid physical properties [*Dyrud et al.*, 2005], are
512 expected to have a strong dependence with latitude [*Dyrud et al.*, 2011]. Because these
513 echoes are also detected by SAAMER, its location will provide valuable new information
514 regarding this phenomena. These results are under current analysis and will be presented
515 in a future paper.

516 Finally, over the past decade, there has been a controversy regarding the differences in
517 measured velocity distributions and consequently orbital distributions of meteors result-
518 ing from HPLA head echo and meteor radar specular trail detections. These differences
519 are in part due to different observational biases introduced by the detection of different
520 scattering mechanisms using an assorted class of radars. The fact that we can perform
521 measurements of all these mechanisms simultaneously with the same instrument will un-
522 doubtedly contribute to clarification of these issues.

523 **Acknowledgments.** This work was supported by NSF Awards AGS - 0634650, AGS -
524 0944104 and AST - 0908118, as well as NASA awards 12-PAST12-0007 and 12-PATM12-

525 0006. We wish to thank the EARG personnel for their invaluable help with the operation
526 of SAAMER. The authors wishes to thank M. Nicolls, S. Close and J. Chau for invaluable
527 discussions.

References

- 528 Baggaley, W. (2002), Radar observations, in *Meteors in the Earth's Atmosphere*, edited
529 by E. Murad and I. Williams, pp. 123–148, Cambridge University Press.
- 530 Brown, P., and J. Jones (1995), A Determination of the Strengths of the Sporadic Radio-
531 Meteor Sources, *Earth Moon and Planets*, 68, 223–245, doi:10.1007/BF00671512.
- 532 Brown, P., R. J. Weryk, D. K. Wong, and J. Jones (2008), The Canadian Meteor Or-
533 bit Radar Meteor Stream Catalogue, *Earth Moon and Planets*, 102, 209–219, doi:
534 10.1007/s11038-007-9162-6.
- 535 Campbell-Brown, M. D. (2008a), Directional Variation of Sporadic Meteor Activity and
536 Velocity, *Earth Moon and Planets*, 102, 79–84, doi:10.1007/s11038-007-9152-8.
- 537 Campbell-Brown, M. D. (2008b), High resolution radiant distribution and orbits of spo-
538 radic radar meteoroids, *Icarus*, 196, 144–163, doi:10.1016/j.icarus.2008.02.022.
- 539 Ceplecha, Z., J. Borovička, W. Elford, D. Revelle, R. Hawkes, V. Porubčan, and M. Šimek
540 (1998), Meteor phenomena and bodies, *Space Sci. Rev.*, 84, 327–471.
- 541 Chau, J. L., and R. Woodman (2004), Observations of meteor head-echoes using the
542 jicamarca 50 mhz radar in interferometer mode, *Atmos. Chem. Phys.*, 3(6), 6063–6091.
- 543 Chau, J. L., R. F. Woodman, and F. Galindo (2007), Sporadic meteor sources as ob-
544 served by the Jicamarca high-power large-aperture VHF radar, *Icarus*, 188, 162–174,
545 doi:10.1016/j.icarus.2006.11.006.

- 546 Close, S., M. Oppenheim, S. Hunt, and A. Coster (2004), A technique for calculating
547 meteor plasma density and meteoroid mass from radar head echo scattering, *Icarus*,
548 *168*, 43–52, doi:10.1016/j.icarus.2003.11.018.
- 549 Close, S., M. Oppenheim, D. Durand, and L. Dyrud (2005), A new method for determining
550 meteoroid mass from head echo data, *Journal of Geophysical Research (Space Physics)*,
551 *110*(A9), 9308–+, doi:10.1029/2004JA010950.
- 552 Close, S., R. Volz, R. Loveland, A. Macdonell, P. Colestock, I. Linscott, and M. Op-
553 penheim (2012), Determining meteoroid bulk densities using a plasma scatter-
554 ing model with high-power large-aperture radar data, *Icarus*, *221*, 300–309, doi:
555 10.1016/j.icarus.2012.07.033.
- 556 Close, S., S. and Hunt, M. Minardi, and F. McKeen (2000), Analysis of perseid meteor
557 head echo data collected using the advance research project agency long-range tracking
558 and instrumentation radar (altair), *Radio Sci.*, *35*(5), 1233–1240.
- 559 Currie, T., J. Debes, T. J. Rodigas, A. Burrows, Y. Itoh, M. Fukagawa, S. J. Kenyon,
560 M. Kuchner, and S. Matsumura (2012), Direct Imaging Confirmation and Character-
561 ization of a Dust-enshrouded Candidate Exoplanet Orbiting Fomalhaut, *Ap. J.*, *760*,
562 L32, doi:10.1088/2041-8205/760/2/L32.
- 563 Dyrud, L., D. Wilson, S. Boerve, J. Trulsen, H. Pecseli, S. Close, C. Chen, and Y. Lee
564 (2007a), Plasma and Electromagnetic Simulations of Meteor Head Echo Radar Reflec-
565 tions, *Earth Moon and Planets*, pp. 65–+, doi:10.1007/s11038-007-9189-8.
- 566 Dyrud, L., D. Wilson, S. Boerve, J. Trulsen, H. Pecseli, S. Close, C. Chen, and Y. Lee
567 (2007b), Plasma and electromagnetic wave simulations of meteors, *Adv. Sp. Res.*, doi:
568 10.1016/j.asr.2007.03.048.

- 569 Dyrud, L. P., and D. Janches (2008), Modeling the meteor head-echo using Arecibo ob-
570 servations, *J. Atmos. Sollar Terr. Phys.*, *70*, 1621, doi:doi:10.1016/j.jastp.2008.06.016.
- 571 Dyrud, L. P., M. M. Oppenheim, S. Close, and S. Hunt (2002), Interpretation of non-
572 specular radar meteor trails, *Geophys. Res. Lett.*, *29*(21), 210,000–1.
- 573 Dyrud, L. P., L. Ray, M. Oppenheim, S. Close, and K. Denney (2005), Modelling
574 high-power large-aperture radar meteor trails, *Journal of Atmospheric and Terrestrial*
575 *Physics*, *67*, 1171–1177, doi:10.1016/j.jastp.2005.06.016.
- 576 Dyrud, L. P., J. Urbina, J. T. Fentzke, E. Hibbit, and J. Hinrichs (2011), Global vari-
577 ation of meteor trail plasma turbulence, *Annales Geophysicae*, *29*, 2277–2286, doi:
578 10.5194/angeo-29-2277-2011.
- 579 Evans, J. V. (1965), Radio-echo studies of meteors at 68-centimeter wavelength, *J. Geo-*
580 *phys. Res.*, *70*, 5395–5416, doi:10.1029/JZ070i021p05395.
- 581 Fentzke, J. T., and D. Janches (2008), A semi-empirical model of the contribution from
582 sporadic meteoroid sources on the meteor input function observed at arecibo, *Journal*
583 *of Geophysical Research (Space Physics)*, *113*(A03304), doi:10.1029/2007JA012531.
- 584 Fentzke, J. T., D. Janches, and J. J. Sparks (2009), Latitudinal and Seasonal Variability
585 of the Micrometeor Input Function: A Study Using Model Predictions, Arecibo, and
586 PFISR Observations, *J. Atmos. Solar Terr. Phys.*, *71*, 653.
- 587 Fritts, D., et al. (2010a), Southern Argentina Agile Meter Radar (SAAMER): System
588 design and initial measurements of large-scale winds and tides, *JGR-Atmospheres*, p.
589 Accepted.
- 590 Fritts, D. C., D. Janches, and W. K. Hocking (2010b), Southern Argentina Agile Meteor
591 Radar: Initial assessment of gravity wave momentum fluxes, *Journal of Geophysical*

- 592 *Research (Atmospheres)*, 115, 19,123–+, doi:10.1029/2010JD013891.
- 593 Fritts, D. C., D. Janches, W. K. Hocking, N. J. Mitchell, and M. J. Taylor (2012a),
594 Assessment of gravity wave momentum flux measurement capabilities by meteor radars
595 having different transmitter power and antenna configurations, *Journal of Geophysical*
596 *Research (Atmospheres)*, 117, D10108, doi:10.1029/2011JD017174.
- 597 Fritts, D. C., D. Janches, H. Iimura, W. K. Hocking, J. V. Bageston, and N. M. P.
598 Leme (2012b), Drake Antarctic Agile Meteor Radar first results: Configuration and
599 comparison of mean and tidal wind and gravity wave momentum flux measurements
600 with Southern Argentina Agile Meteor Radar, *Journal of Geophysical Research (Atmo-*
601 *spheres)*, 117, D02105, doi:10.1029/2011JD016651.
- 602 Galligan, D. P., and W. J. Baggaley (2004), The orbital distribution of radar-detected
603 meteoroids of the Solar system dust cloud, *Month. Not. R. Astron. Soc.*, 353, 422–446,
604 doi:10.1111/j.1365-2966.2004.08078.x.
- 605 Galligan, D. P., and W. J. Baggaley (2005), The radiant distribution of AMOR radar me-
606 teors, *Month. Not. R. Astron. Soc.*, 359, 551–560, doi:10.1111/j.1365-2966.2005.08918.x.
- 607 Gardner, C. S., X. Chu, P. Espy, J. Plane, D. Marsh, and D. Janches (2011), Seasonal
608 variations of the mesospheric Fe layer at Rothera, Antarctica , *Journal of Geophysical*
609 *Research (Atmospheres)*, 116, D02,304, doi:10.1029/2010JD014655.
- 610 Hey, J. S., S. J. Parsons, and G. S. Stewart (1947), Radar observations of the Giacobinids
611 meteor shower, 1946, *Month. Not. R. Astr. Soc.*, 107, 176.
- 612 Hocking, W. K., T. Thayaparan, and J. Jones (1997), Meteor decay times and their use in
613 determining a diagnostic mesospheric Temperature-pressure parameter: Methodology
614 and one year of data, *Geophys. Res. Lett.*, 24, 2977–2980, doi:10.1029/97GL03048.

- 615 Hocking, W. K., B. Fueller, and B. Vandeppeer (2001), Real-time determination of meteor-
616 related parameters utilizing modern digital technology, *J. Atmos. Solar Terr. Phys*, *63*,
617 155–169.
- 618 Hunt, S., M. Oppenheim, S. Close, P. Brown, F. McKeen, and M. Minardi (2004), De-
619 termination of the meteoroid velocity distribution at the earth using high-gain radar,
620 *Icarus*, *168*.
- 621 Janches, D., and D. ReVelle (2005), The initial altitude of the micrometeor phenomenon:
622 Comparison between arecibo radar observations and theory, *J. Geophys. Res.*, *110*.
- 623 Janches, D., J. Mathews, D. Meisel, V. Getman, and Q. Zhou (2000a), Doppler studies
624 of near-antapex uhf radar micrometeors, *Icarus*, *143*, 347–353.
- 625 Janches, D., J. Mathews, D. Meisel, and Q. Zhou (2000b), Micrometeor observations using
626 the arecibo 430 mhz radar: I. determination of the ballistic parameter from measured
627 doppler velocity and deceleration results, *Icarus*, *145*, 53–63.
- 628 Janches, D., A. Pellinen-Wannberg, G. Wannberg, A. Westman, I. Haggstrom, and
629 D. Meisel (2002), Tristatic observations of meteors using the 930 mhz eiscat radar
630 system, *J. Geophys. Res.*, *107*(A11), 1389, doi:10.1029/2001JA009,205.
- 631 Janches, D., M. Nolan, D. Meisel, J. Mathews, Q. Zhou, and D. Moser (2003), On
632 the geocentric micrometeor velocity distribution, *J. Geophys. Res.*, *108*(A6), 1222,
633 doi:10.1029/2002JA009,789.
- 634 Janches, D., M. Nolan, and M. Sulzer (2004), Radiant measurement accuracy of mi-
635 crometeors detected by the arecibo 430 mhz dual-beam radar, *Atmos. Chem. Phys.*, *4*,
636 621–626.

- 637 Janches, D., D. C. Fritts, D. M. Riggin, M. P. Sulzer, and S. Gonzalez (2006), Gravity
638 waves and momentum fluxes in the MLT using 430MHz dual-beam measurements at
639 Arecibo: 1. Measurements, methods, and gravity waves, *J. Geophys. Res.*, *111*, doi:
640 10.1029/2005JD006882.
- 641 Janches, D., C. Heinselman, J. Chau, A. Chandran, and R. Woodman (2006), Modeling
642 the global micrometeor input function in the upper atmosphere observed by high power
643 and large aperture radars, *J. Geophys. Res.*, *111*.
- 644 Janches, D., S. Close, and J. T. Fentzke (2008), A comparison of detection sensitiv-
645 ity between ALTAIR and Arecibo meteor observations: Can high power and large
646 aperture radars detect low velocity meteor head-echoes, *Icarus*, *193*, 105–111, doi:
647 10.1016/j.icarus.2007.08.022.
- 648 Janches, D., L. P. Dyrud, S. L. Broadley, and J. M. C. Plane (2009), First observation of
649 micrometeoroid differential ablation in the atmosphere, *Geophys. Res. Lett.*, *36*, 6101–+,
650 doi:10.1029/2009GL037389.
- 651 Janches, D., J. L. Hormaechea, E. Gularte, C. Brunini, W. K. Hocking, and D. Fritts
652 (2012), An initial meteoroid stream survey in the southern hemisphere using the South-
653 ern Argentina Agile Meteor Radar (SAAMER), *Icarus*, p. Under review.
- 654 Johansen, A., J. S. Oishi, M.-M. Mac Low, H. Klahr, T. Henning, and A. Youdin (2007),
655 Rapid planetesimal formation in turbulent circumstellar disks, *Nature*, *448*, 1022–1025,
656 doi:10.1038/nature06086.
- 657 Jones, J., and P. Brown (1993), Sporadic meteor radiant distribution: Orbital survey
658 results, *Mon. Not. R. Astron. Soc.*, *265*, 524–532.

- 659 Jones, J., A. R. Webster, and W. K. Hocking (1998), An improved interferometer design
660 for use with meteor radars., *Radio Science*, *33*, 55–65, doi:10.1029/97RS03050.
- 661 Kero, J., C. Szasz, A. Pellinen-Wannberg, G. Wannberg, A. Westman, and D. D. Meisel
662 (2008), Determination of meteoroid physical properties from tristatic radar observations,
663 *Annales Geophysicae*, *26*, 2217–2228, doi:10.5194/angeo-26-2217-2008.
- 664 Kero, J., C. Szasz, T. Nakamura, D. D. Meisel, M. Ueda, Y. Fujiwara, T. Terasawa,
665 H. Miyamoto, and K. Nishimura (2011), First results from the 2009-2010 MU radar
666 head echo observation programme for sporadic and shower meteors: the Orionids 2009,
667 *Month. Not. R. Astron. Soc.*, *416*, 2550–2559, doi:10.1111/j.1365-2966.2011.19146.x.
- 668 Kliore, A. J., et al. (2008), First results from the Cassini radio occultations of the Ti-
669 tan ionosphere, *Journal of Geophysical Research (Space Physics)*, *113*, A09317, doi:
670 10.1029/2007JA012965.
- 671 Lau, E. M., S. K. Avery, J. P. Avery, D. Janches, S. E. Palo, R. Schafer, and N. A.
672 Makarov (2006), Statistical characterization of the meteor trail distribution at the South
673 Pole as seen by a VHF interferometric meteor radar, *Radio Science*, *41*, 4007–+, doi:
674 10.1029/2005RS003247.
- 675 Malhotra, R. (1995), The Origin of Pluto’s Orbit: Implications for the Solar System
676 Beyond Neptune, *Astron. J.*, *110*, 420, doi:10.1086/117532.
- 677 Mathews, J. D., D. D. Meisel, K. P. Hunter, V. S. Getman, and Q. Zhou (1997), Very
678 High Resolution Studies of Micrometeors Using the Arecibo 430 MHz Radar, *Icarus*,
679 *126*, 157–169, doi:10.1006/icar.1996.5641.
- 680 Mathews, J. D., D. Janches, D. Meisel, and Q. Zhou (2001), The micrometeoroid mass
681 flux into the upper atmosphere: Arecibo results and a comparison with prior estimates,

- 682 *Geophys. Res. Lett.*, 28(10), 1929–1932.
- 683 McKinley, D. W. R. (1961), *Meteor Science and Engineering*, 1–309 pp., McGraw Hill,
684 New York.
- 685 Nesvorný, D., P. Jenniskens, H. F. Levison, W. F. Bottke, D. Vokrouhlický, and
686 M. Gounelle (2010), Cometary Origin of the Zodiacal Cloud and Carbonaceous Microm-
687 eteorites. Implications for Hot Debris Disks, *Ap. J.*, 713, 816–836, doi:10.1088/0004-
688 637X/713/2/816.
- 689 Nesvorný, D., D. Janches, D. Vokrouhlický, P. Pokorný, W. F. Bottke, and P. Jenniskens
690 (2011a), Dynamical Model for the Zodiacal Cloud and Sporadic Meteors, *Ap. J.*, 743,
691 129, doi:10.1088/0004-637X/743/2/129.
- 692 Nesvorný, D., D. Vokrouhlický, P. Pokorný, and D. Janches (2011b), Dynamics of Dust
693 Particles Released from Oort Cloud Comets and Their Contribution to Radar Meteors,
694 *Ap. J.*, 743, 37, doi:10.1088/0004-637X/743/1/37.
- 695 Okamoto, Y. K., et al. (2004), An early extrasolar planetary system revealed by planetes-
696 imal belts in β Pictoris, *Nature*, 431, 660–663, doi:10.1038/nature02948.
- 697 Pätzold, M., S. Tellmann, B. Häusler, D. Hinson, R. Schaa, and G. L. Tyler (2005),
698 A Sporadic Third Layer in the Ionosphere of Mars, *Science*, 310, 837–839, doi:
699 10.1126/science.1117755.
- 700 Pätzold, M., S. Tellmann, B. Häusler, M. K. Bird, G. L. Tyler, A. A. Christou, and
701 P. Withers (2009), A sporadic layer in the Venus lower ionosphere of meteoric origin,
702 *Geophys. Res. Lett.*, 36, L05203, doi:10.1029/2008GL035875.
- 703 Pellinen-Wannberg, A., and G. Wannberg (1994), Meteor observations with the Eu-
704 ropean incoherent scatter UHF radar, *J. Geophys. Res.*, 99, 11,379–11,390, doi:

705 10.1029/94JA00274.

706 Pifko, S., D. Janches, S. Close, J. J. Sparks, T. Nakamura, and D. Nesvorný (2012),
707 MODELING THE METEOROID INPUT FUNCTION AT MID-LATITUDE USING
708 METEOR OBSERVATIONS BY THE MU RADAR, *Icarus*, doi:Submitted.

709 Plane, J. (2003), Atmospheric chemistry of meteoric metals, *Chem. Rev.*, *103*(12), 4963–
710 4984.

711 Plane, J., W. Feng, D. Marsh, D. Janches, M. Chipperfield, J. P. Burrows, and M. Sinnhu-
712 ber (2010), Towards a global model of the meteoric metal layers, in *38th COSPAR*
713 *Scientific Assembly, COSPAR, Plenary Meeting*, vol. 38, pp. 1511–+.

714 Sato, T., T. Nakamura, and K. Nishimura (2000), Orbit determination of meteors using
715 the mu radar, *IEICE Trans. Commun.*, *E83-B*(9).

716 Sparks, J. J., D. Janches, M. J. Nicolls, and C. J. Heinselman (2009), Seasonal and Diurnal
717 Variability of the meteor flux at high latitudes observed using PFISR, *J. Atm. Solar*
718 *Terr. Phys.*, *71*, 644, doi:10.1016/j.jastp.2008.08.009.

719 Sparks, J. J., D. Janches, M. J. Nicolls, and C. Heinselman (2010), Determination of
720 physical and radiant meteor properties using PFISR interferometry measurements of
721 head echoes, *Journal of Atmospheric and Solar-Terrestrial Physics*, *72*, 1221–1230, doi:
722 10.1016/j.jastp.2010.08.004.

723 Walsh, K. J., A. Morbidelli, S. N. Raymond, D. P. O’Brien, and A. M. Mandell (2011),
724 A low mass for Mars from Jupiter’s early gas-driven migration, *Nature*, *475*, 206–209,
725 doi:10.1038/nature10201.

726 Wiegert, P., J. Vaubaillon, and M. Campbell-Brown (2009), A dynamical model of the
727 sporadic meteoroid complex, *Icarus*, *201*, 295–310, doi:10.1016/j.icarus.2008.12.030.

728 Withers, P., M. Mendillo, D. P. Hinson, and K. Cahoy (2008), Physical characteristics
729 and occurrence rates of meteoric plasma layers detected in the Martian ionosphere by
730 the Mars Global Surveyor Radio Science Experiment, *Journal of Geophysical Research*
731 (*Space Physics*), *113*, A12314, doi:10.1029/2008JA013636.

732 Younger, J. P., I. M. Reid, R. A. Vincent, D. A. Holdsworth, and D. J. Murphy (2009),
733 A southern hemisphere survey of meteor shower radiants and associated stream orbits
734 using single station radar observations, *Month. Not. R. Astr. Soc.*, *398*, 350–356, doi:
735 10.1111/j.1365-2966.2009.15142.x.

736

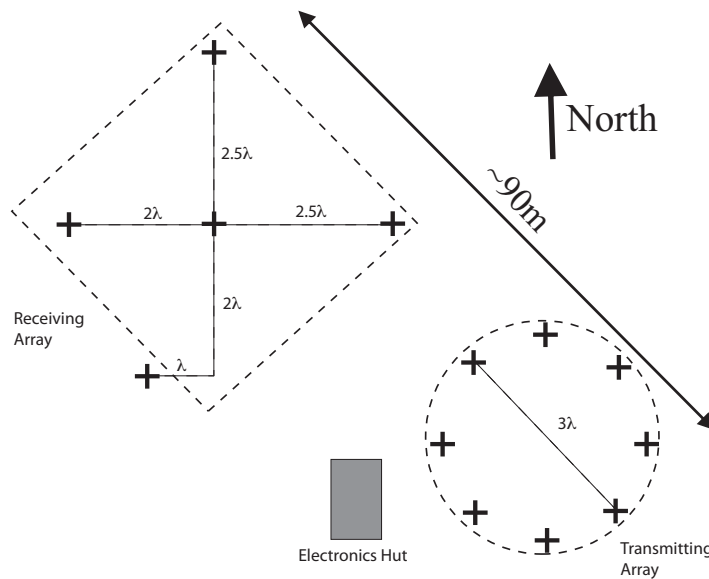


Figure 1. Antenna transmitter and receiver layout at Rio Grande, Tierra del Fuego (with individual antennas indicated with plus symbols).

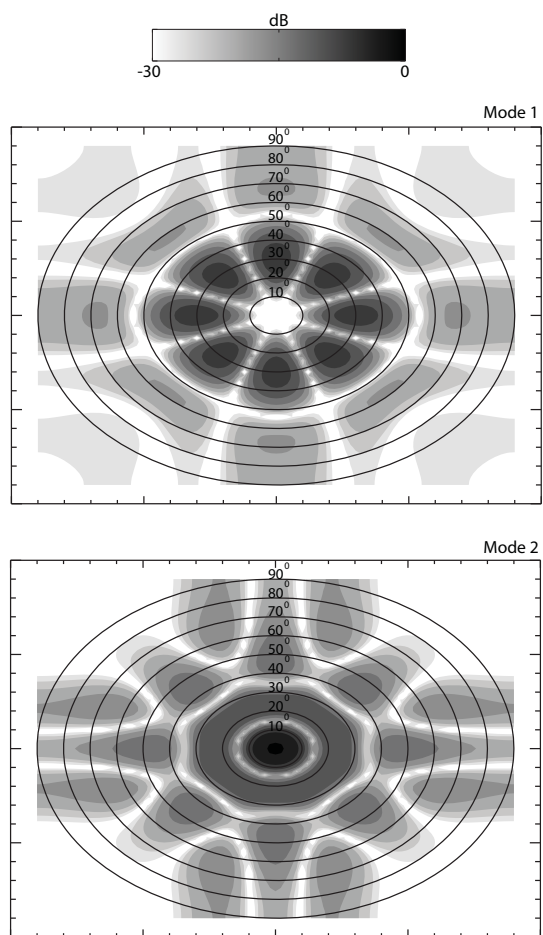


Figure 2. SAAMER's radiation patterns transmitting a) Mode 1: 180° off phase and b) Mode 2: all antennas in phase.

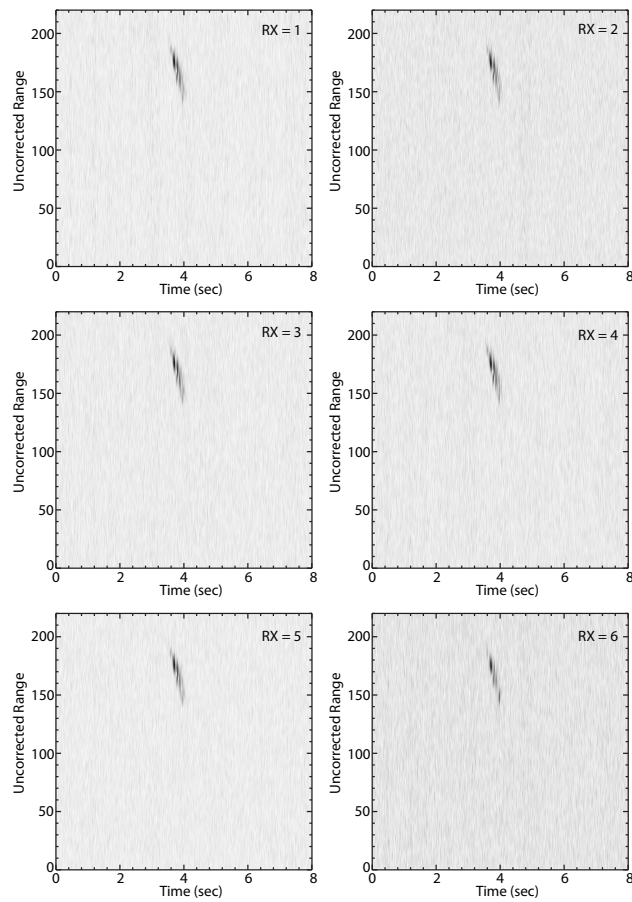


Figure 3. RTI Images of a head echo event observed by SAAMER. The first 5 panels represent the signal detected by each of the receiving antennas while the last panel displays the signal recorded by the transmitting array utilized as a receiver.

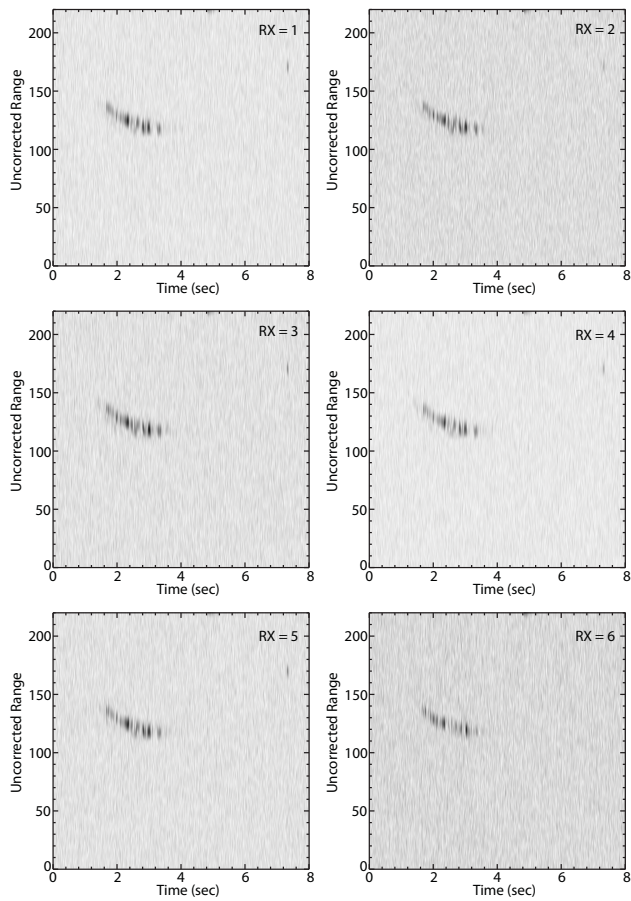


Figure 4. Same as Figure 3 for a second event which also displays the beginning of a specular trail.

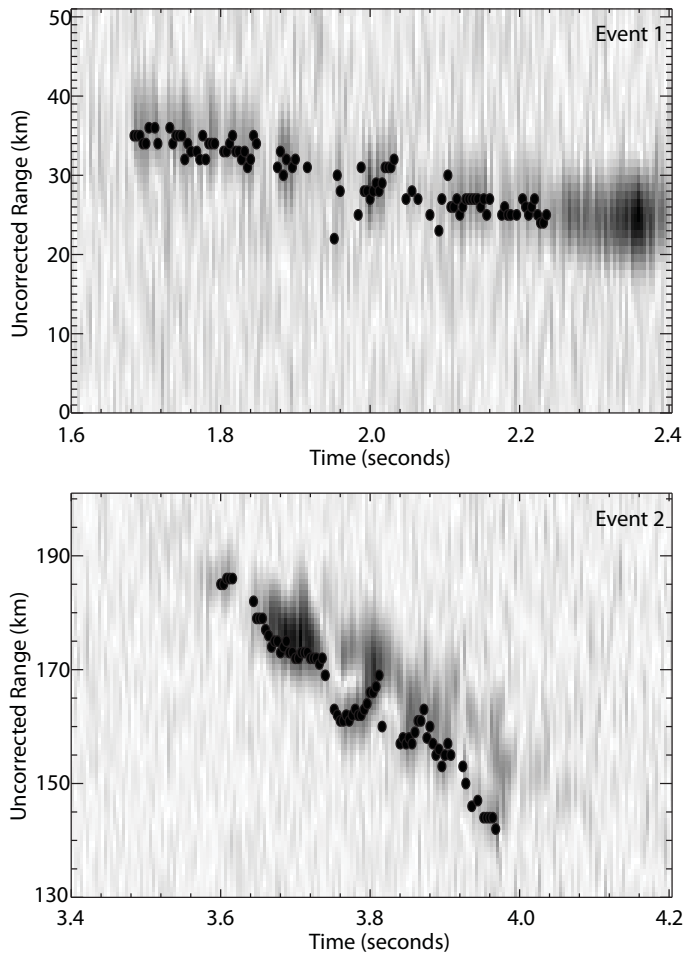


Figure 5. Detail RTI images of the events displayed in Figures 3 and 4. The black dots show the range gates that were utilized for interferometric calculation purposes.

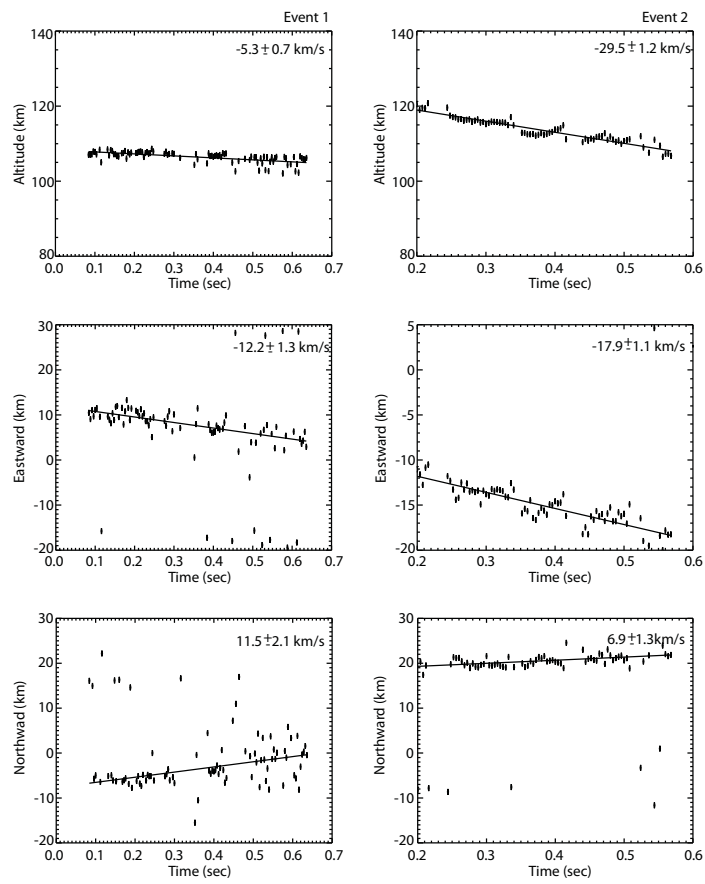


Figure 6. Interferometric spatial and velocity determinations of the events displayed in Figures 3 and 4.

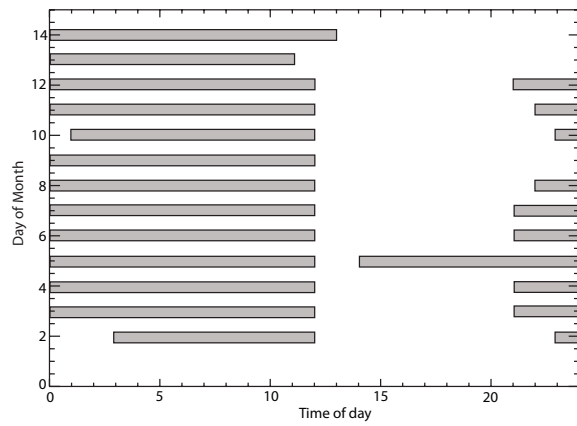


Figure 7. SAAMER's observing periods for the head echo experiment performed in August 2011.

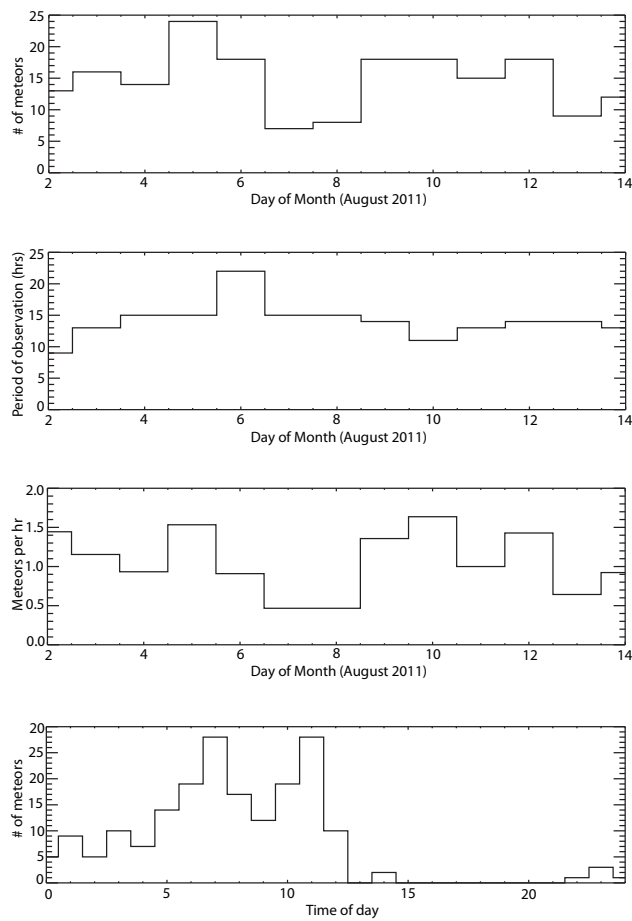


Figure 8. a) Number of meteors detected per day of observations; b) number of observed hours per day of observation; c) average number of meteors per hours observed; and d) number of meteors observes as a function of time of the day with all days compiled.

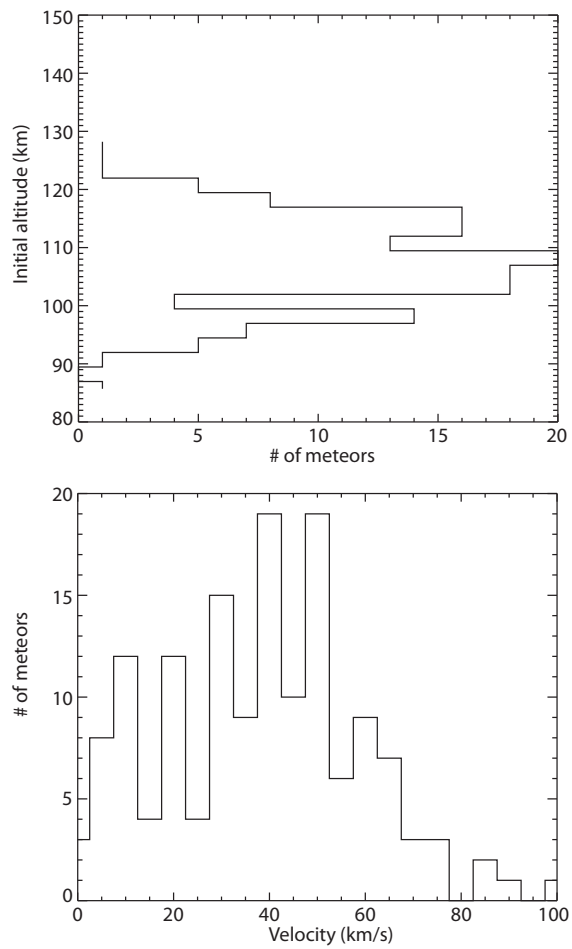


Figure 9. Top panel: observed initial altitude distribution; bottom panel: Observed absolute velocity distribution.

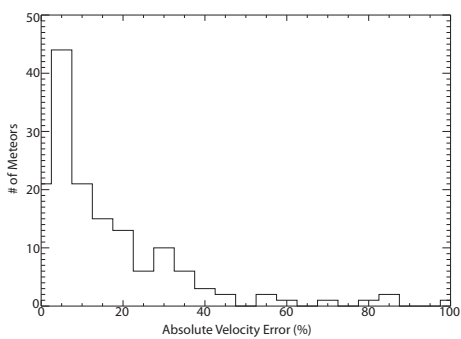


Figure 10. Distribution of calculated errors on the velocity determination

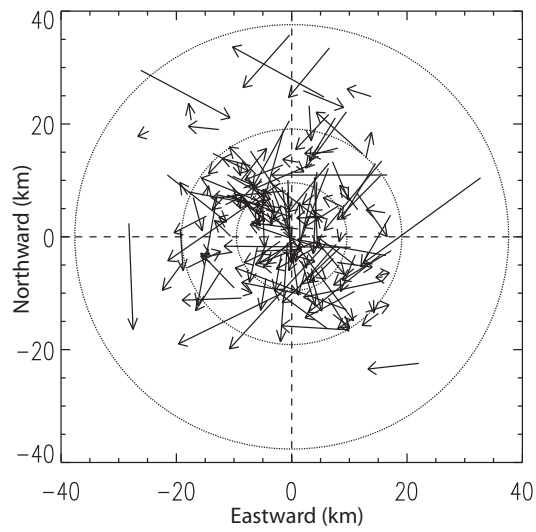


Figure 11. Horizontal projections of the vector velocities displays as arrows. The circles represent 5, 10 and 20 degrees off zenith at 110 km of altitude.

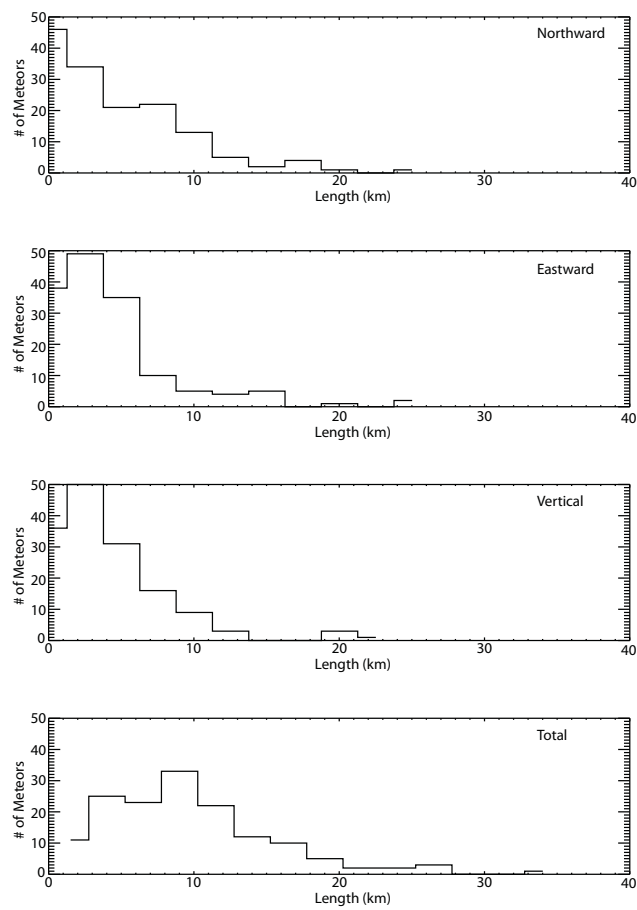


Figure 12. Top three panels display the distribution of the spatial coverage of the head echo events in the three directions. The bottom panel displays the distribution of the absolute observed displacement.

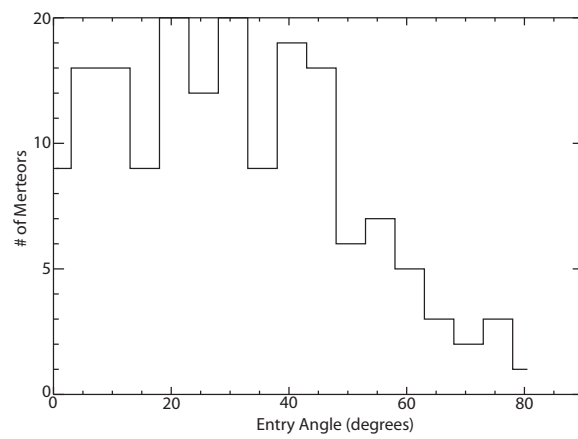


Figure 13. Distribution of calculated entry angle measure from the local Zenith.

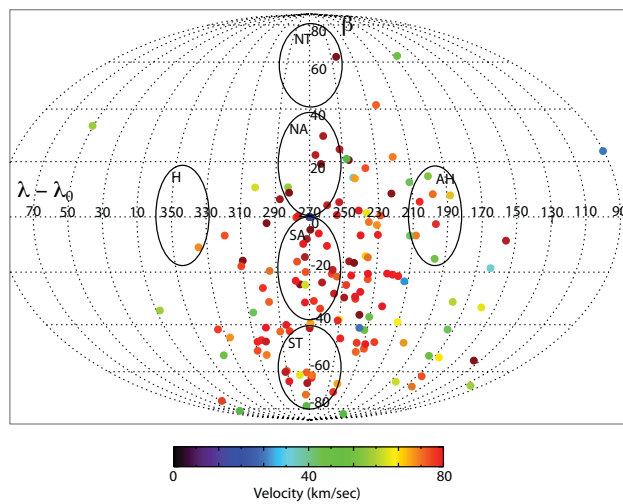


Figure 14. Calculated meteoroid radiant color coded to their velocity plotted in terms of Sun-centered ecliptic longitude ($\lambda - \lambda_0$) and latitude (β). The ellipses represent the location of the six apparent sporadic meteoroid sources.

Quantity (units)	
Latitude (degrees)	53.8°
Longitude (degrees)	67°
Frequency (MHz)	32.55
PRF (Hz)	500
Peak Transmitted Power (kW)	60
Banwidth (MHz)	0.05
Coherent Integrations (# of IPP)	2
Pulse Code	Monopulse
Pulse Length (μs)	13.6
Sampling Resolution (m)	250
FWHM	8°

Table 1. SAAMER’s Operating characteristics for Head-Echo mode

RADAR	λ (m)	f (MHz)	P_t (kW)	Aperture (m ²)	G (dB)	P_d (W/m ²)
SAAMER	9.7	32.55	60	74	10	5×10^{-6}
MU	6.5	46	1000.	8332.3	34	0.02
Jicamarca	6	50	2000	90,000	45	0.5
ALTAIR	1.8	160	6000	6648	44	1.23
Arecibo	0.69	430	2000	70,686	63	28.9
PFISR	0.68	440	1500	866.25	43	0.3

Table 2. Comparison of various figures of merit between SAAMER and HPLA radars

Mass (\log_{10} g)	Minimum Speed (km/s)				
	MU	ALTAIR	Arecibo	PFISR	SAAMER
-7	80	40	25	–	–
-6	60	25	15	25	–
-5	25	15	5	15	–
-4	10	All	All	All	60
-3	10	All	All	All	40
-2	All	All	All	All	15

Table 3. Minimum meteoroid speed required for radar detection as a function of meteoroid mass for several HPLA radar systems reproduced from *Pifko et al.* [2012]